Bioactive Materials 19 (2023) 268–281

Contents lists available at ScienceDirect

Bioactive Materials

journal homepage: www.keaipublishing.com/en/journals/bioactive-materials

Tissue-specific melt electrowritten polymeric scaffolds for coordinated regeneration of soft and hard periodontal tissues

Arwa Daghrery [a,b], Jessica A. Ferreira [a], Jinping Xu [a], Nasim Golafshan [c,d], Darnell Kaigler [e], Sarit B. Bhaduri [f,g], Jos Malda [c,d,h], Miguel Castilho [c,d,i,j,**], Marco C. Bottino [a,k,*]

[a] Department of Cariology, Restorative Sciences, and Endodontics, School of Dentistry, University of Michigan, Ann Arbor, MI, United States
[b] Department of Restorative Dental Sciences, School of Dentistry, Jazan University, Jazan, Kingdom of Saudi Arabia
[c] Department of Orthopedics, University Medical Center Utrecht, Utrecht, the Netherlands
[d] Regenerative Medicine Center, Utrecht, the Netherlands
[e] Department of Periodontics and Oral Medicine, School of Dentistry, University of Michigan, Ann Arbor, MI, United States
[f] Department of Mechanical, Industrial and Manufacturing Engineering, University of Toledo, Toledo, OH, United States
[g] EEC Division, Directorate of Engineering, The National Science Foundation, Alexandria, VA, United States
[h] Department of Clinical Sciences, Faculty of Veterinary Medicine, Utrecht University, Utrecht, the Netherlands
[i] Department of Biomedical Engineering, Eindhoven University of Technology, Eindhoven, the Netherlands
[j] Institute for Complex Molecular Systems, Eindhoven University of Technology, P.O. Box 513, 5600 MB Eindhoven, the Netherlands
[k] Department of Biomedical Engineering, College of Engineering, University of Michigan, Ann Arbor, MI, United States

ARTICLE INFO

Keywords:
Periodontitis
Melt electrowriting
3D printing
Inflammation
Periodontal regeneration
Scaffold

ABSTRACT

Periodontitis is a chronic inflammatory condition that often causes serious damage to tooth-supporting tissues. The limited successful outcomes of clinically available approaches underscore the need for therapeutics that cannot only provide structural guidance to cells but can also modulate the local immune response. Here, three-dimensional melt electrowritten (*i.e.*, poly(ε-caprolactone)) scaffolds with tissue-specific attributes were engineered to guide differentiation of human-derived periodontal ligament stem cells (hPDLSCs) and mediate macrophage polarization. The investigated tissue-specific scaffold attributes comprised fiber morphology (aligned vs. random) and highly-ordered architectures with distinct strand spacings (small 250 μm and large 500 μm). Macrophages exhibited an elongated morphology in aligned and highly-ordered scaffolds, while maintaining their round-shape on randomly-oriented fibrous scaffolds. Expressions of periostin and IL-10 were more pronounced on the aligned and highly-ordered scaffolds. While hPDLSCs on the scaffolds with 500 μm strand spacing show higher expression of osteogenic marker (Runx2) over 21 days, cells on randomly-oriented fibrous scaffolds showed upregulation of M1 markers. In an orthotopic mandibular fenestration defect model, findings revealed that the tissue-specific scaffolds (*i.e.*, aligned fibers for periodontal ligament and highly-ordered 500 μm strand spacing fluorinated calcium phosphate [F/CaP]-coated fibers for bone) could enhance the mimicking of regeneration of natural periodontal tissues.

1. Introduction

Periodontitis is a highly prevalent chronic inflammatory, bacteria-triggered oral pathology affecting 47% of adults with 30 years of age and older. From a therapeutic standpoint, if not properly treated, periodontitis causes severe destruction of the periodontal attachment apparatus (*i.e.*, the alveolar bone, periodontal ligament [PDL], and cementum), ultimately leading to tooth loss [1,2]. A vast body of knowledge reveals that there are no effective approaches for reliably regenerating periodontal defects with severe bone loss, and thus

Peer review under responsibility of KeAi Communications Co., Ltd.

* Corresponding author. Regenerative Dentistry University of Michigan School of Dentistry Department of Cariology, Restorative Sciences, and Endodontics 1011 N. University (Room 5223), Ann Arbor, MI, 48109, USA.

** Corresponding author. Biomaterials Design and Processing Eindhoven University of Technology & University Medical Center Utrecht De Rondom 70, 5612, AP Eindhoven, the Netherlands. .

E-mail addresses: m.dias.castilho@tue.nl (M. Castilho), mbottino@umich.edu (M.C. Bottino).

https://doi.org/10.1016/j.bioactmat.2022.04.013
Received 21 December 2021; Received in revised form 14 March 2022; Accepted 13 April 2022
Available online 22 April 2022

avoiding tooth extraction [3]. Specifically, contemporary approaches to treat periodontitis involve thorough subgingival scaling and root planing, open flap surgery, and guided tissue regeneration by means of a degradable membrane that, while serving as a barrier against soft tissue infiltration, allows resident progenitor cells to promote the regeneration of periodontal tissues [2]. Collectively, despite the evidence that some level of periodontal regeneration (*e.g.*, new alveolar bone, cementum, and PDL) may occur following the aforementioned therapeutics [4], the ability to mimic native periodontal tissues may be impractical in many clinical situations, due to the multi-tissue complexity and three-dimensional (3D) nature of periodontal defects [3].

It is well-established that periodontal regeneration requires simultaneous management of both soft (PDL) and hard tissue interfaces [3]. Importantly, the acquisition of well-oriented PDL fibers with alveolar bone regeneration is paramount [3,5]. It has been postulated that, *in vivo*, effective tissue integration can be enabled through the fabrication of tissue-specific scaffold layouts to recreate the relationship between structure and function – the key to engineering the natural hard-to-soft tissue interface [6]. From this perspective, additive manufacturing (AM), a rapidly evolving field that uses a layer-by-layer deposition process to develop structurally tailored scaffolds, has been implemented in regenerative dental medicine [3,7,8]. The pivotal data in periodontics using Selective Laser Sintering (SLS), a successful AM technique, disappointingly showed its inability to obtain structures with a degradation profile matching that of bone and PDL neoformation [9]. The bulky nature of SLS and fused deposition modeling (FDM) scaffolds and the fact that soft and hard periodontal tissues regenerate at distinct rates, emphasize the need for scaffolds with well-defined tissue-specific attributes [3,7,8]. Indeed, previous attempts to encourage the regeneration of periodontal tissues through multiphasic/biphasic scaffolds to address the multi-tissue nature of the periodontium have been reported [10–13]. However, the challenges of multi-tissue regeneration, require a number of requirements to consider tissue-specific characteristics such as differences in volume, architecture, cell type, and structural properties to recapitulate the regeneration of its soft-to-hard tissue interfaces [3,7,8].

Melt ElectroWriting (MEW) has been introduced as an alternative AM process that enables the production of fibrous scaffolds with well-defined macro- and microstructural features, such as porosity (*i.e.*, strand spacing), and fiber alignment and diameter [14]. This control over structural features offers great promise to match tissue-specific characteristics [3,15] supporting the spatiotemporal events that could ultimately allow concomitant regeneration of soft (PDL) and hard (cementum and alveolar bone) periodontal tissues. Up until now, FDA-approved polymers that are inherently hydrophobic and do not promote tissue regeneration, such as poly(ε-caprolactone) (PCL), remain the most widely used for MEW. Coating strategies, for instance, with bioceramics, have been used to improve the osteogenic capacity of PCL scaffolds [16,17]. Noteworthy, although fluorinated calcium phosphate (F/CaP)-coated MEW polymeric fibrous scaffolds enable substantial alveolar bone regeneration while supporting PDL neoformation [15], recent literature states that monophasic scaffolding strategies are limited in their ability to recreate the angular structure of PDL at the bone–ligament interface [18,19]. These recent results further highlight the need for personalized (*i.e.*, defect- and tissue-specific) solutions that can guide the coordinated growth and development of the periodontal attachment apparatus.

In recent years, scaffold-mediated strategies that provide 3D templates and biomimetic extracellular matrix (ECM) microenvironments while concurrently guiding body's immune responses have been suggested for tissue engineering applications [20]. The innate immune response plays an important role after implantation of biomaterials to mitigate the pro-inflammatory reaction and allows macrophage polarization [21]. Pro-inflammatory M1 macrophage conversion to anti-inflammatory macrophage (M2) phenotype is critical in the overall inflammatory response at the site of biomaterial implantation [20]. Thus, biomaterial-mediating scaffolds are equivalent, if not a possible alternative, for presently used soluble biomolecules in directing the response of progenitor cells to promote tissue healing and, ultimately, regeneration [20,22]. Given the fact that biomaterials can effectively be used to guide complex tissue regeneration and/or modulate the inflammatory response after periodontal tissue destruction; we hypothesize that a scaffold with dual functions that support coordinated growth of alveolar bone and PDL through well-defined macroarchitecture (*i.e.*, strand spacing), composition (F/CaP coating), and microstructural features (fiber alignment) and, at the same time, modulates the immune response to amplify in situ tissue regeneration can be fabricated.

To test our hypothesis, in this investigation, we utilized MEW to engineer uniquely tailored fibrous scaffolds at defined fiber orientations (randomly-oriented or aligned scaffolds) and strand spacings (*i.e.*, a crosshatch pattern of fibers with strand spacings of 500 μm and 250 μm; hereafter referred to as highly-ordered scaffolds). The effects of fiber orientation and strand spacing on human-derived periodontal ligament stem cells' (hPDLSCs) attachment/proliferation, and differentiation were examined *in vitro* to define the most favorable PDL-specific region in a zonal, tissue-specific scaffold for periodontal reconstruction. Collectively, we explored a versatile and innovative platform (*i.e.*, MEW) that could ultimately lead to the development of zonal smart biomaterial scaffolds capable of directing tissue-specific (aligned fibers for PDL and highly-ordered 500 μm strand spacing fluorinated calcium phosphate [F/CaP]-coated fibers for alveolar bone) stem cell differentiation and macrophage polarization as a potential personalized therapy for effective periodontal tissue regeneration.

2. Materials and methods

2.1. Chemicals and materials

Poly(ε-caprolactone) (PCL, Mn: 5000, CELLINK, Göthenburg, Sweden) was used. All other reagents were procured from Sigma-Aldrich (St. Louis, MO, USA), unless otherwise specified: sodium hydroxide (NaOH, ≥ 98%), potassium fluoride (KF ≥ 99.90%), ethanol (99.50%), ethylenediaminetetraacetic acid calcium disodium salt (EDTA-Ca), potassium phosphate (KH_2PO_4 ≥ 99%), hexamethyldisilazane (HMDS ≥99%), ascorbic acid-2 phosphate, hexadecylpyridinium chloride monohydrate (CPC), and paraformaldehyde (PFA). Distilled-deionized (DI) water was prepared using a Milli-Q® ultrapure water system (MilliporeSigma, Burlington, MA, USA) and utilized in all experiments. Phosphate-buffered saline (PBS) was obtained from GIBCO-Invitrogen (Carlsbad, CA, USA). Heat-inactivated fetal bovine serum (15% FBS) solution, a 1% penicillin–streptomycin solution, and alfa-minimum essential medium (α-MEM), were bought from HyClone (Gibco/Life Technologies Corp., Grand Island, NY, USA). Collagen type I PhotoCol® (Lot#8292) was purchased from Advanced BioMatrix (San Diego, CA, USA).

2.2. Melt electrowriting (MEW) and scaffold designs

Poly(ε-caprolactone) MEW scaffolds were fabricated in a biosafety cabinet using a multi-head 3D (bio)printing platform (3DDiscovery, regenHU Ltd., Villaz-St-Pierre, Switzerland). Briefly, polymer pellets were loaded into the metal cartridge overlaid with a 26G nozzle, then heated at 90 °C for 30 min to form a homogeneous polymer melt, and subsequently dispensed at 0.07 MPa system's pressure [16]. Scaffolds with aligned fiber orientation and 0/90°crosshatch designs were printed at parameters of 40 mm/s feed rate and 7 kV applied voltage. Randomly-oriented fibers were printed at 0.1 MPa system's pressure, 40 mm/s feed rate, and 10 kV voltage. The 0/90°crosshatch laydown pattern has 500 μm strand spacing or 250 μm strand spacing. Of note, the referred aligned fibrous scaffolds have a major strand at 0° of 250 μm spacing and densely packed aligned fibers designed with 100 μm strands spacing at 90°. All scaffolds were produced at 4 mm distance from the collector, at room temperature (RT) ~21.5 °C and 38.5% humidity level.

The tissue-specific (zonal) scaffolds utilized in the *in vivo* model were designed to form a construct encompassing 800 layers for the bone zone and 200 layers for the PDL zone. All scaffold designs and respective G-codes were generated using BioCAD and accompanying bioprinter software. As formerly established, in order to improve hydrophilicity of the PCL, the scaffolds were treated with NaOH [23]. First, the scaffolds were soaked in 70% ethanol for 15 min, and then they were submerged in a 5 M NaOH solution at RT for 4 h [15]. To neutralize the pH, the scaffolds were rinsed thoroughly with DI water and left to air-dry overnight. To enhance the bioactivity of the PCL fibers of the bone compartment, they were modified with a fluorinated calcium phosphate (F/CaP) coating following our previously reported protocol [15]. Finally, the scaffolds were sterilized using 70% ethanol and UV-irradiated (30 min/side) for all experiments [15].

2.3. Morphological and chemical analyses

The structural characterization of the scaffolds (0/90°crosshatch with 500 μm or 250 μm strand spacings, aligned, and randomly-oriented fibrous scaffolds) were assessed using a scanning electron microscope (SEM, MIRA3, FEG-SEM, TESCAN Brno, Kohoutovice, Czech Republic). For chemical analysis, Fourier transformed infrared spectroscopy (16 scans with spectra between 4000 and 600 cm^{-1} at 4 cm^{-1} resolution) in the Attenuated Total Reflectance mode (ATR-FTIR, Thermo-Nicolet iS-50, Thermo Fisher Scientific Inc., Waltham MA, USA) was performed. FTIR spectra were baseline-corrected and normalized for analysis.

2.4. Cell culture

Human periodontal ligament (hPDL) tissues were harvested from the middle segment of the tooth root surface as previously reported [24]. Briefly, freshly obtained tissues were cultured on alpha-minimum essential medium (α-MEM), then the PDL cells were collected, centrifuged, and resuspended at 37 °C for 60 min in solution containing PBS, 2 mg/mL collagenase type II, and 4 mg/mL dispase II. The mixture was inactivated using α-MEM containing FBS and 100 μM ascorbic acid 2 phosphate. The cells were allowed to grow in T25 flasks and passaged for further experiments (passage specified below).

2.5. Flow cytometry

In order to assess the presence and expression of mesenchymal stem cell (MSC) surface markers, flow cytometry (MA900 Cell Sorter, Sony Biotechnology Inc., San Jose, CA, USA) was performed following the criteria recommended by the Mesenchymal and Tissue Stem Cell Committee of the International Society of Cellular Therapy (ISCT): CD45, CD90, CD105, CD34 [24,25]. Human-derived periodontal ligament stem cells (hPDLSCs) were harvested from T75 flasks, washed with PBS, and incubated with blocking solution, followed by incubation with specific antibodies conjugated with a fluorochrome, PE anti-human CD90 antibody, FITC anti-human CD34 antibody, APC anti-human CD105, and APC-H7 anti-human CD44 antibody. Then, samples were washed and placed in 100 μL PBS followed by analysis. The collected data were analyzed using FlowJo software (FlowJo, Treestar Inc., Ashland, OR, USA).

2.6. Cell proliferation

Human-derived PDLSCs at passage 5 were harvested and seeded on scaffolds (8 × 8 mm^2) at a density of 6 × 10^4 in 24-well low-attachment plates (Corning Life Sciences, Tewksbury, MA, USA) and cultured in α-MEM supplemented with 15% FBS and 1% penicillin-streptomycin solution. The plates were incubated in an atmosphere of 95% relative humidity and 5% CO_2 at 37 °C. To determine hPDLSCs proliferation, the 3-(4,5-dimethylthiazol-2-yl)-5(3-carboxymethonyphenol)-2-(4-sulfophenyl)-2H-tetrazolium (MTS) calorimetric assay (CellTiter 96 AQueous One Solution Assay, Promega Corporation, Madison, WI, USA) was performed at selected time points over 7 days. At predetermined time points, the cells were incubated for 2 h with the MTS solution according to the manufacturer's instructions, followed by measuring the absorbance in a microplate reader at 490 nm (SpectraMax iD3; Molecular Devices LLC, San Jose, CA, USA).

2.7. Macrophage polarization

RAW 264.7 cells (TIB-71, American Type Culture Collection, Manassas, VA, USA) at passage 4, were used. The cells were harvested using a cells' scraper and seeded on square-shaped (8 × 8 mm^2) scaffolds at a density of 6 × 10^4 cells/scaffold in 24-well low-attachment plates (Corning Life Sciences) and cultured in DMEM high-glucose medium supplemented with 10% FBS, in an atmosphere of 5% CO_2 and 95% humidity at 37 °C, followed by qPCR and ELISA as detailed below.

2.8. Cell/scaffold interaction

Confluent hPDLSCs and RAW 264.7 cells at passage 5 were harvested and cultured on the four distinct scaffolds (500 μm or 250 μm strand spacings, aligned, and randomly-oriented fibrous scaffolds). Briefly, 6 × 10^4 cells/scaffold were seeded and cultured for 3 and 7 days. For SEM assessment, 4% PFA for 48 h at 4 °C was used to fix the cells. Then, the scaffolds were subjected to ascending ethanol concentrations (up to 100%) for dehydration, followed by overnight incubation in HMDS. Lastly, the cell-laden scaffolds were mounted on Al stubs using double-sided adhesive carbon tape, and then sputter-coated with Au for 70 s (SPI-Module Carbon/Sputter Coater, Thermo Fisher Scientific Inc., West Chester, PA, USA) prior to imaging. For fluorescence evaluation, hPDLSCs were fixed in 4% PFA as mentioned above, and then washed (3 ×) in PBS. The cells were then treated with 0.1% Triton X-100 for 5 min. After rinsing with PBS (2 ×), the cell-laden scaffolds were blocked using 1.5% bovine serum albumin (BSA) in PBS for 30 min, followed by staining with TRITC-conjugated phalloidin and DAPI (1:1200, Millipore Sigma) for 1 h at RT. Finally, the cell-laden scaffolds were carefully rinsed (3 ×) in PBS to wash out any excess of phalloidin conjugate and positioned on a glass slide for imaging (Eclipse-Ti, Nikon Corporation, Tokyo, Japan).

2.9. mRNA expressions using qPCR

The expression of commonly probed ligamentogenic (Periostin – POSTN, Hs01566750_m1, Scleraxis – SCX, Hs03054634_g1, and Collagen III – Col3, Hs00943809_m1), and osteogenic (Runt-related transcription factor 2 – Runx2, Hs01047973_m1) genes were analyzed by means of quantitative polymerase chain reaction (qPCR). Glyceraldehyde 3-phosphate dehydrogenase (GAPDH, Hs02758991_g1) was utilized as the housekeeping gene. For macrophage polarization, M1 markers, IL-1 receptor ligands (IL1, Mm00434228), M2 markers IL-10 receptor ligands (IL-10, Il10 Mm01288386 M1), and mannose receptor CD206 (MRC1, Mm01288386) were analyzed at days 1, 3, and 7. In brief, the cells were harvested, and the total RNA was isolated (Purelink RNA Mini Kit, Invitrogen Corporation), followed by cDNA synthesis using iScript RT Supermix (Bio-Rad Laboratories, Inc., Hercules, CA, USA). Finally, the delta-Cq method was applied to measure the relative amount of gene expression from the quantification cycle (Cq) values retrieved by qPCR analysis. qPCR results were normalized to the reference sample.

2.10. Cytokine quantification via mouse quantikine ELISA kit

IL1β, IL-6, and IL-10 cytokine release levels of LPS-stimulated macrophages cultured on the various scaffolds were evaluated using the Mouse Quantikine ELISA Kit (R&D Systems, Inc., Minneapolis, MN, USA), following the manufacturer's protocol. The cytokines level was

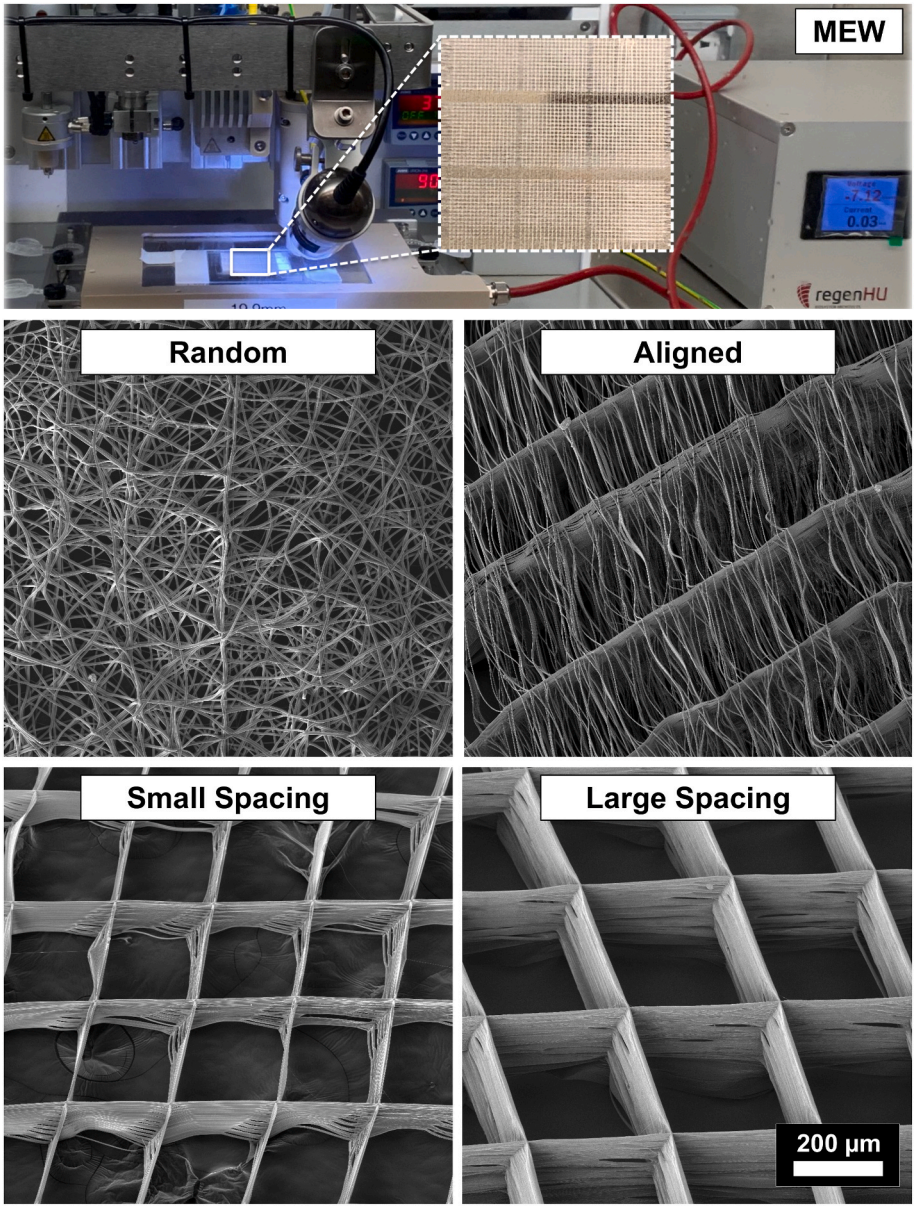

Fig. 1. Melt electrowriting (MEW) setup to fabricate fibrous scaffolds of distinct fiber configuration and highly-ordered architectures. Representative SEM images of the various MEW PCL scaffolds show melt electrowritten polymeric (*i.e.*, poly(ε-caprolactone) scaffolds with tissue-specific attributes such as fiber morphology (random vs. aligned) and highly-ordered (0°/90° crosshatch pattern) architecture with distinct strand spacings (small 250 μm and large 500 μm). Overall, the as-produced scaffolds display fiber diameters (in μm) ranging from 2.3 ± 0.1, 2.5 ± 0.2, 2.6 ± 0.3 and 4.2 ± 0.7 and porosity of 52.9%, 91.7%, 85.5 and 30.9% in aligned, large and small strand spacing to randomly-deposited fibers, respectively.

measured using the supernatants extracted at days 1, 3, and 7. The absorbance was measured on a plate reader (SpectraMax iD3) at 450 nm and corrected with the reference wavelength at 570 nm.

2.11. Periodontal fenestration defect model in rats

All experiments with rats (Fischer 344, Envigo RMS, Inc., Oxford, MI, USA) were conducted in accordance and approved by the University of Michigan Institutional Animal Care and Use Committee (PRO#00008502). Twenty-four 6-week-old male rats (300–320 g) were used in this study. For surgical procedures, general anesthesia was induced with 4–5% isoflurane inhalation (Piramal Critical Care Inc., Bethlehem, PA, USA) and preserved at a concentration between 1 and 3%. Subsequently, periodontal fenestration defects were created surgically at 2 × 3 mm (height × width) and 1 mm in depth in the rat mandible. In detail, alveolar bone, followed by cementum and soft tissue components around the tooth root, were removed. The distinct scaffolds (n = 6/group/time point) were assigned according to the following groups: (1) Sham – no treatment, (2) Collagen, (3) Tissue-specific zonal scaffolds with bone and PDL zone, and (4) Tissue-specific zonal scaffolds infused with collagen. For preparation of the tissue-specific MEW PCL scaffolds infused with collagen, a collagen type I solution (3 mg/mL) was dissolved in acetic acid. Subsequently, the solution was neutralized using a neutralization agent provided in the kit (Advanced BioMatrix). Then, the collagen infused scaffolds were allowed to gellate at 37 °C for 30 min inside the incubator. All scaffolds were implanted in the artificially-created defects and periodontal tissue regeneration evaluated after 3 and 6 weeks of healing. At the predetermined time points post-implantation, the mandibles were retrieved and fixed in formalin prior to micro-computed tomography (microCT), histological, and immunological analyses.

2.12. Micro-computed tomography and histological analyses

Regenerated alveolar bone at each periodontal defect was evaluated using a Scanco microCT scanner (SCANCO Medical μCT 100, SCANCO Medical AG, Brüttisellen, Switzerland), following a 360° rotation scan at 70 kV, 114 μA monochromatic x-rays and 25 μm voxel sizes. The frames' exposure time was kept at 500 ms on average. To reconstruct the 3D images of the defect area, SCANCO Medical System software was used.

Briefly, the reconstructed 3D image was utilized to outline the original defect area (hereafter referred to as the region of interest, ROI). For each sample, ROI was analyzed to quantify the following parameters: bone volume (BV, mm^3), bone fill (BF%, BV/TV), and tissue mineral density (TMD, $mgHA/cm^3$). Following microCT scans, the mandibles of each group were decalcified in 10% EDTA for 3 weeks. Upon decalcification, the samples were dehydrated in an ascending series of alcohol and then embedded in paraffin before cutting into 4-μm sections for Masson's trichrome (MT) staining. The slides were then imaged using a light microscope equipped with a digital camera (Nikon E800, Nikon Corporation) to determine mineralized bone formation.

2.13. Immunofluorescence analysis

Sections (4 μm-thick) were dewaxed at 60 °C for 15 min, then rehydrated in ethanol gradients. Of note, to reduce endogenous peroxidase activity, the sections were stored in 3% H_2O_2 for 20 min at RT. For blocking unspecific binding, the slides were immersed in 3% BSA for 10 min at RT, followed by incubation with primary antibodies: *anti*-periostin (rabbit polyclonal, ab14041, Abcam, Cambridge, MA, USA) (dilution 1:500) overnight at 4 °C. The slides were then incubated with Alexa-conjugated secondary antibodies: Alexa Flour goat anti-rabbit IgG (H + L) (dilution 1:200) for 1 h at RT. Then, a drop of vectashield antifade mounting media with DAPI was added to the slide to visualize the cell nuclei. The untreated lingual side of the distal root of the same tooth was used as control for visualization of native PDL tissues for comparison purposes. The negative controls section was incubated in PBS instead of the primary antibody. The images were obtained at 4 × and 20 × for *anti*-periostin (Nikon E800, Nikon Corporation).

2.14. Moving toward clinical translation – accuracy of MEW personalized scaffolds

To design personalized (*i.e.*, defect-specific) scaffolds, a standardized periodontal fenestration defect as described earlier was scanned using microCT (SCANCO Medical μCT 100, SCANCO Medical AG, Brüttisellen, Switzerland), with the aforementioned scanning parameters. The CAD design to obtain personalized scaffolds was achieved using SolidWorks software from the CT scan images. Upon assessment of the scaffold geometry, BioCAM™ software was used to define the scaffold internal architecture and subsequently translate the design into a G-Code. Designed scaffolds were fabricated using the previously detailed MEW platform (3DDiscovery, RegenHU) with the optimized printing parameters. Next, the printing accuracy (n = 3) of the personalized scaffolds was quantified as reported previously [26]:

$$\text{Printing accuracy} = \frac{V_p}{V_{CS}}$$

Where Vp and Vcs represent the circumference of the personalized scaffold and CAD designed scaffolds, respectively. The circumferences of the two geometries were measured with Meshlab (v. 2016). The printing accuracy is defined from 0 to 1, which 1 shows the highest printing accuracy of the scaffolds.

2.15. Statistics

GraphPad Prism 5 software package (GraphPad Software, San Diego, CA, USA) was used to carry out statistical analyses of the data. Unless otherwise specified, data are presented as Mean ± SD. Group comparisons were performed using one-way or two-way ANOVA, followed by Tukey's multiple comparison post-hoc test. A two-sided 5% statistical significance level was employed in all tests.

3. Results and discussion

3.1. Processing and characterization of MEW PCL scaffolds

MEW was successfully employed in manufacturing 3D fibrous scaffolds with distinct designs, namely highly-ordered (*i.e.*, crosshatch 0/90°) with 250 μm (small) and 500 μm strand spacing (large), as well as with highly-oriented (aligned) and non-oriented (random) fiber configurations (Fig. 1). Obtained scaffolds were highly porous and

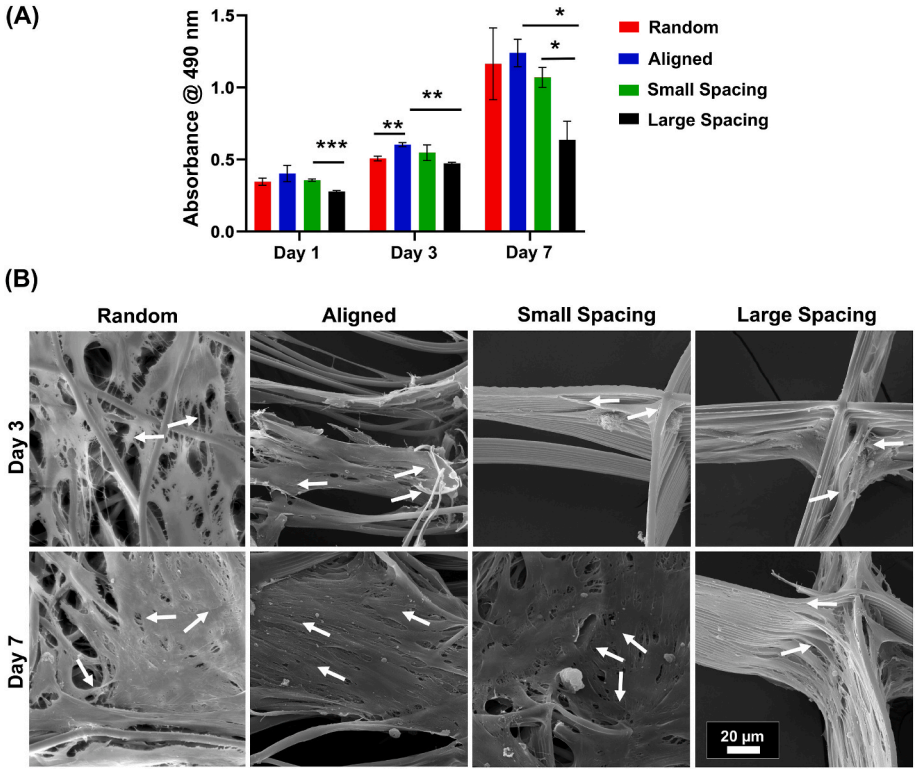

Fig. 2. Attachment and proliferation of hPDLSCs on MEW PCL scaffolds with aligned and randomly oriented fiber configurations, and 250 μm and 500 μm strand spacings. **(A)** Cell viability of hPDLSCs seeded on the scaffolds using AlamarBlue assay over 7 days. **(B)** Representative SEM images of hPDLSCs proliferation on the scaffolds after 3 and 7 days. Note the characteristic cell stretch along the fibrous walls (All SEM images have the same scale bar). A more pronounced spreading was detected along the scaffolds with randomly oriented fibers (white arrows indicate the direction of filopodia protrusion). (Mean ± SD, n = 3). *p < 0.05, **p < 0.01, ***p < 0.001.

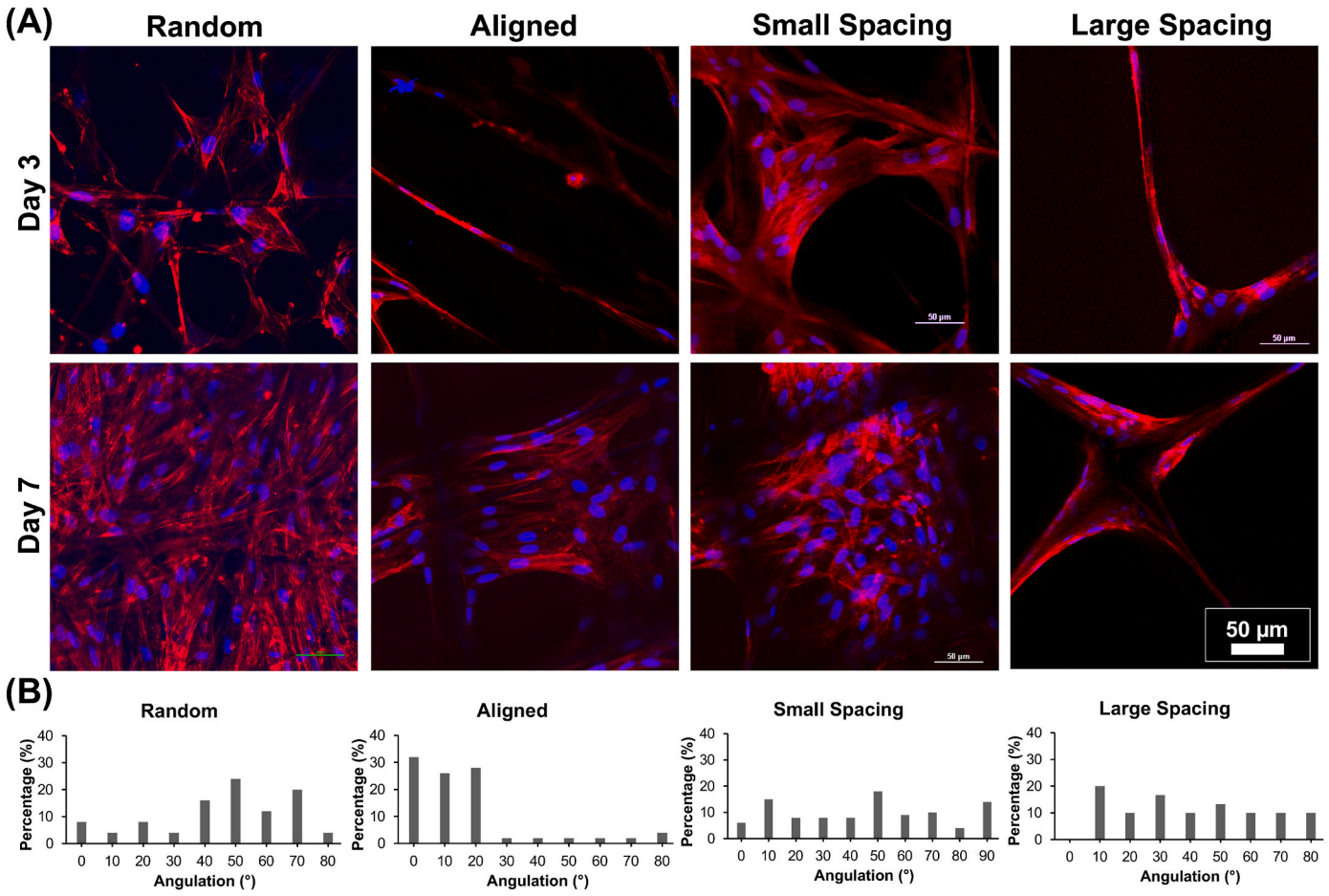

Fig. 3. Patterns of hPDLSCs alignment on the various MEW PCL scaffolds. (A) Representative CLSM images show a variable pattern of cells' bridging, following the fibers' arrangements at day 3 and 7. DAPI (blue) and phalloidin (red) fluorescent staining (scale bar = 50 µm). **(B)** Histograms of PDLSCs nucleus angulation on scaffolds with aligned and randomly oriented fiber configurations as well as crosshatch 0/90° arrangement and 250 µm and 500 µm strand spacings corresponding to confocal images.

presented a smooth fiber morphology. Despite the traditional MEW fabrication process usually produces organized scaffold architectures, arbitrary deposition of PCL fibers over the collecting plate by simply adjusting the interplay between voltage and mass flow rates (*i.e.*, 10 kV and 0.1 MPa pressure), resulted in non-oriented, random fibrous scaffolds. These random scaffolds displayed an overall porosity of 30.9% comparable to those observed in conventional solution electrospinning [27]. On the other hand, by decreasing the strands spacing down to 100 µm, the remaining electrical charges within fibers started to create repelling forces [28]. The repelling forces were advantageous to prevent fiber stacking, and thus the as-formed scaffolds exhibited aligned fibers supported by the main strands at 0°, which was critical in maintaining the 3D structural characteristic of the scaffolds. Meanwhile, highly-ordered scaffold architectures displaying small (250 µm) and large (500 µm) strand spacings were created with homogeneous interconnected porosity by carefully optimizing key instrument parameters (*i.e.*, electric voltage, pressure, feed rate, and adequate strand spacing). Overall, the as-produced polymeric scaffolds display fiber diameters ranging from 2.3 ± 0.1 µm to 4.2 ± 0.7 µm and porosity from 30.9% to 91.7% (Fig. 1).

3.2. hPDLSCs alignment and differentiation depends on fiber orientation and scaffold architecture

Specific alignments of fibrous tissues at tissue interfaces have vital roles in optimizing biomechanical and biophysical responses [19]. For example, angulated PDLs that anchor the teeth inside the alveolar bone play a key function in the absorption and the distribution of masticatory/occlusal forces. Therefore, a tissue-specific guiding scaffold to encourage the simultaneous regeneration of tooth-ligament-bone interfaces via MEW fabrication of structurally and compositionally tailored zonal scaffolds (*i.e.*, highly-oriented (aligned) fibers for the PDL zone and a highly-ordered (500 µm strand spacing), nanostructured fluorinated CaP-coated porous scaffold for the bone zone) is explored in this investigation.

In order to define the stemness of the hPDLSCs utilized throughout this investigation, the expression of specific MSC surface markers CD90, CD105, and CD44 was evaluated [24]. Following proper isolation and expansion of hPDLSCs, high levels of CD90 (>99.70%), CD105 (>99.96%), and CD 44 (>99.70) were observed (Fig. S1). As expected, our human-derived PDLSCs fail to express the hematopoietic stem cell marker CD34. Previously, it was reported that hPDLSCs are very suitable for the regeneration of the periodontal complex as these cells could differentiate into the osteogenic, fibrogenic, and cementogenic linage [29,30]. The fate of PDLSCs is determined by the local microenvironment, *e.g.*, the presence of biologically active molecules, such as growth factors can direct osteogenic or fibroblastic linage [31]. Equally important, in a biomaterial-based approach, the scaffold architecture and stiffness further steer hPDLSCs' differentiation and maturation [32,33]. Notably, in our study, hPDLSCs responded to the distinct scaffold architectures and fiber configuration in terms of their proliferation and differentiation capacity (Fig. 2). While hPDLSCs seeded on non-oriented (random) and highly-oriented (aligned) fibers show a higher proliferation rate compared to MEW PCL scaffolds with variable strand spacings

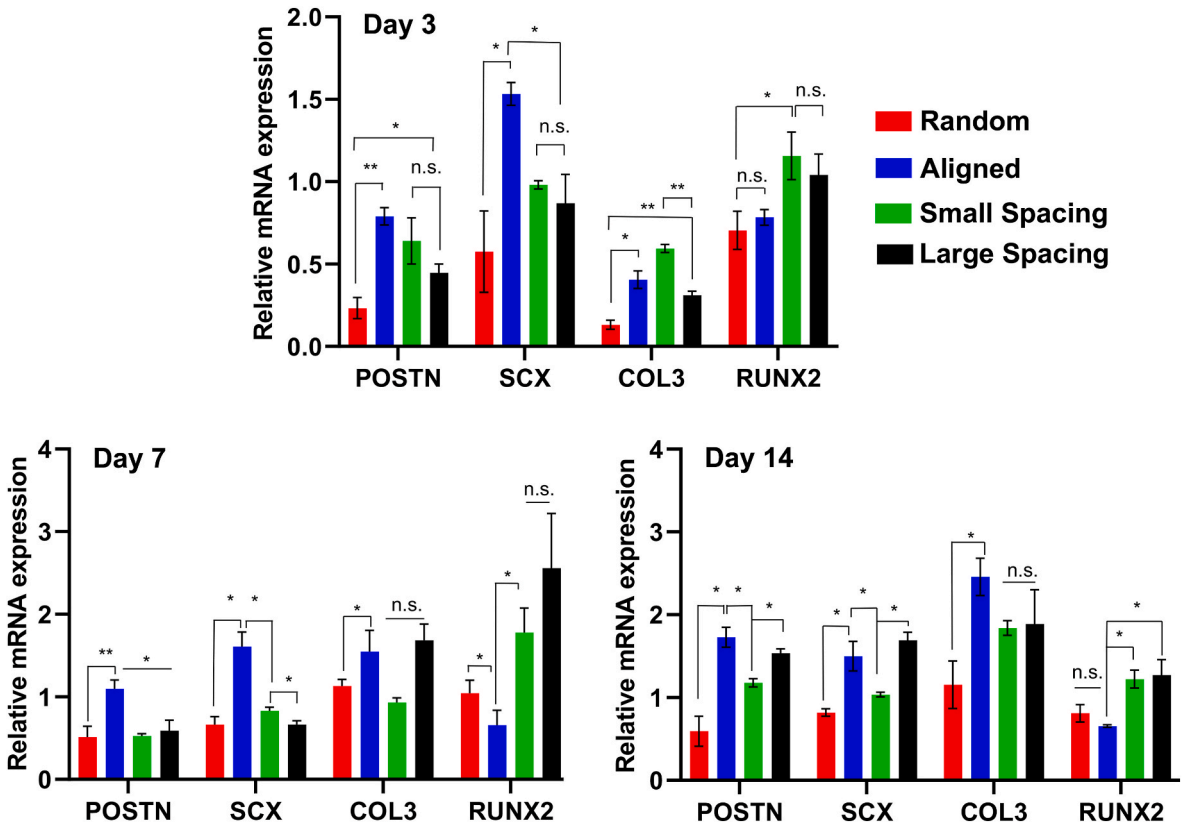

Fig. 4. Ligamentogenic and osteogenic differentiation of hPDLSCs seeded on the various MEW PCL scaffolds. The mRNA levels at days 3, 7, and 14 of selected ligamentogenic genes (i.e., periostin, Scleraxis, and Col3) were significantly higher in scaffolds with aligned fibers, whereas an osteogenic marker (Runx2) was significantly higher in crosshatch 0/90° scaffolds with 250 μm and 500 μm strand spacing. (Mean ± SD, n = 4). *p < 0.05, **p < 0.01.

(Fig. 2A), small strand spacing show a significantly higher proliferation rate compared to large throughout the evaluated *in vitro* culture period (Fig. 2A). These results are in agreement with previously observed proliferation pattern in MEW PCL scaffolds with strand spacings ranging from 500 μm to 1000 μm [15]. This fact is due to the higher surface area and reduced strand spacing (pore size) that, in turn, enhances initial cell attachment.

The direct changes in the morphology of the hPDLSCs related to the contact guidance induced by the various MEW PCL scaffolds are evident through both SEM (Fig. 2B) and fluorescence (phalloidin staining) imaging (Fig. 3). The highly-oriented (aligned) scaffolds with parallelly deposited fibers allow hPDLSCs to align parallel to the direction of fibers' long axes (Fig. 2B), while in random and highly-ordered scaffolds (*i.e.*, small and large strand spacings), hPDLSCs exhibit a polygonal shape, extended cytoskeleton in multiple directions, and disorganized orientation. Interestingly, at day 3, cells start to spread at the corner of individual strands in the highly-ordered patterns of both small and large strand spacings, while at day 7, a more extended cell behavior to fill in between strands is better seen in small strand spacing compared to the larger one (Fig. 3A). Though, in scaffolds with randomly-oriented fibers the nuclei exhibited multi directional angulation dictated by underlying fibers (Fig. 3B), the effect of aligned fibers on the morphology of the hPDLSCs is more dramatic due to contact guidance, which supports an elongated cytoskeleton pattern and nuclei alignment along fiber axes (Fig. 3B). Consequently, the hPDLSCs adopted a typical spindle-shape morphology when cultured on aligned fibers, a characteristic, previously observed for human fibroblasts [34].

To evaluate the differentiation potential of hPDLSCs on the engineered scaffolds, the expression of genes specifically coding for ligamentogenesis (periostin [POSTN], Scleraxis [SXC], and Collagen III [COL3]) and osteogenesis (Runt-related transcription factor 2 [RUNX2] were evaluated in the absence of differentiation factors (Fig. 4). hPDLSCs cultured on the aforementioned scaffolds exhibited different mRNA expression profiles of POSTN, SXC, COL3, and RUNX2. The matricellular protein, POSTN, is highly detected in collagen-rich connective tissues, and its expression reveals integrity and maturation of the periodontal ligament matrix [35,36]. Fiber alignment and strand spacing significantly changed the expression level of POSTN mRNA at day 3, with higher expression in aligned compared to randomly-oriented fibrous scaffolds. At day 7, POSTN expression was upregulated in all scaffolds with a significant increase in the aligned group. In addition, the level of SXC expression, a typical marker of tendogenesis/ligamentogenesis [37], in aligned scaffolds was higher than in the randomly oriented fibrous scaffolds and highly-ordered scaffolds with small and large strand spacings at days 3 and 7 ($P < 0.05$).

While the expression of COL3 in aligned and small strand spacing (250 μm) scaffolds was not significantly different, the expression for the larger (500 μm) strand spacing was significantly lower than former scaffolds with 250 μm strand spacing at day 3 ($P < 0.01$). At day 7, the expression of COL3 increased in highly-ordered scaffolds (small and large strand spacings) and reached comparable levels to the aligned group. It is known that COL3 is the predominant constituent of tendon/ligament-related extracellular matrix (ECM) and contributes to the formation of collagen bundles which are responsible for PDL mechanical properties [35].

Runt-related transcription factor 2 (RUNX2) is known to synchronize osteoblast differentiation and is highly expressed in bone and periodontal ligament [38]. Our findings showed that RUNX2 was generally upregulated at day 3 in highly-ordered scaffolds with small (250 μm) strand spacing and was significantly higher in the randomly-oriented scaffolds. At day 7, RUNX2 expression was upregulated in highly-ordered scaffolds with large strand spacing and downregulated in

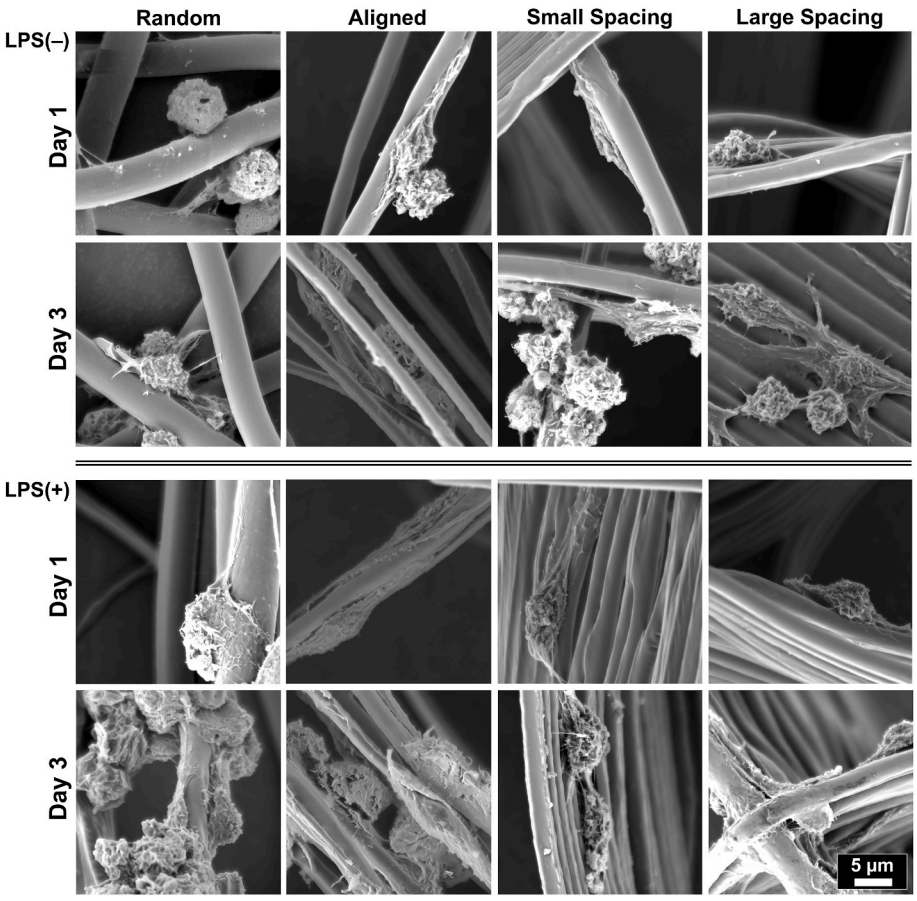

Fig. 5. Representative SEM images showing RAW 264.7 cells' morphology of spontaneously differentiated and LPS-stimulated macrophages. MEW scaffolds with varying fiber orientation and architecture (strand spacing), namely, random, aligned, and scaffolds of 250 μm and 500 μm strands spacing at 0°/90°-oriented junctions. The images show mixed patterns of macrophages spreading, the round shape typical for M1 and more pronounced elongated pattern typical for M2 phenotype.

aligned scaffolds. Noteworthy, although at day 14, the pattern of RUNX2 expression tends to downregulate compared to day 7, it remained significantly higher in small and large spacing scaffolds compared to randomly-oriented and aligned scaffolds ($P < 0.05$). Collectively, increased ligamentogenesis and partially downregulated osteogenesis of hPDLSCs mediated by aligned fibers' configuration were noted. While in the absence of any differentiation factors, the upregulation of osteogenesis markers of hPDLSCs in small and large strand spacing scaffolds is

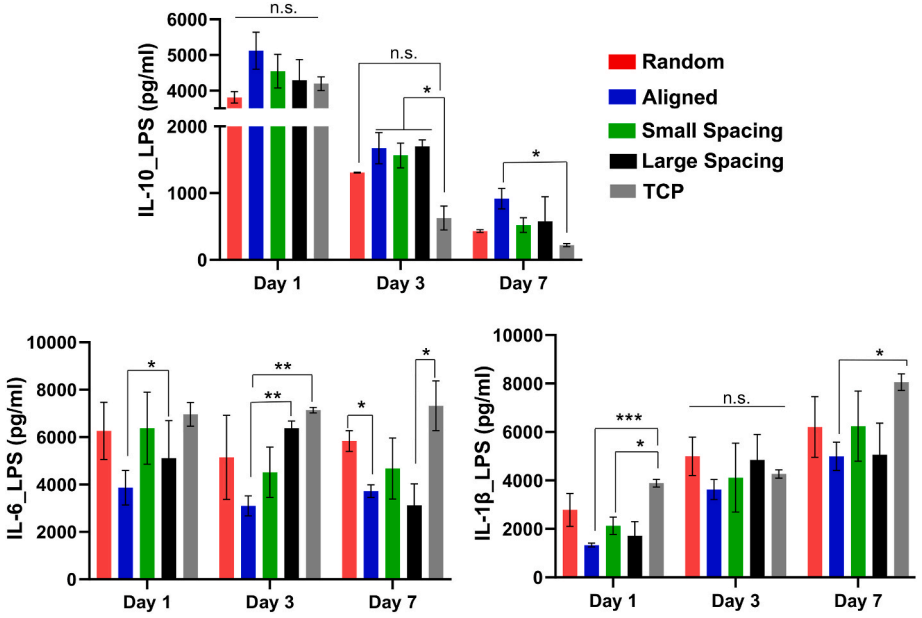

Fig. 6. Cytokine release of LPS-stimulated macrophages on scaffolds with different fiber orientation and architecture (strand spacing). Released cytokines were measured using supernatants extracted after culturing macrophages on different scaffolds, and they were compared to control TCP over 7 days. (Mean ± SD, n = 3). *p < 0.05; **p < 0.01, ***p < 0.001.

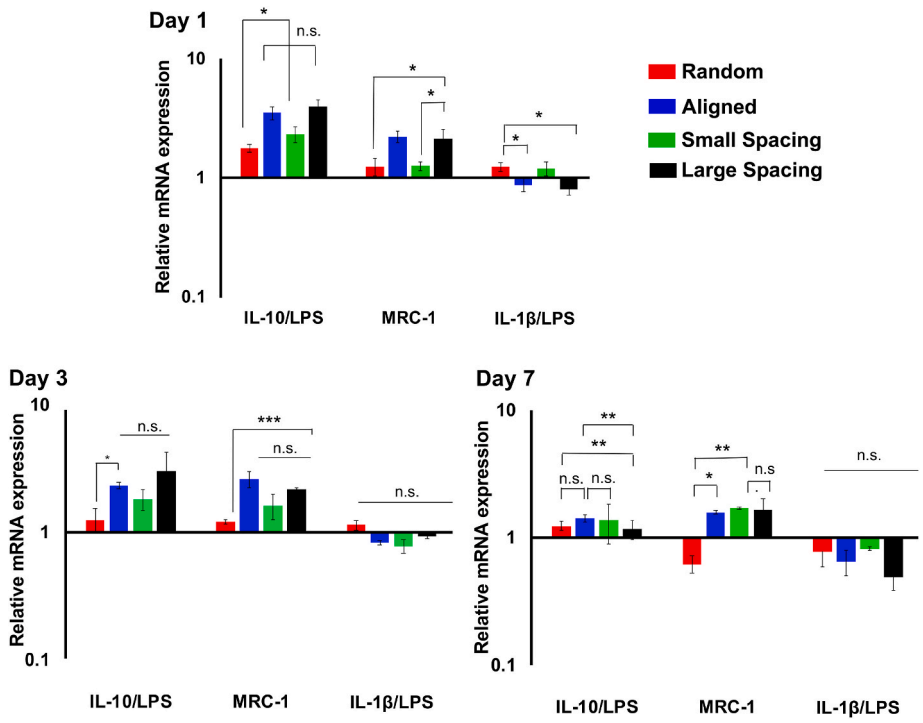

Fig. 7. Gene expression profile of LPS-stimulated macrophages, the level of IL-10, MRC1 and IL-1β. Expression of specific markers was measured using qPCR for M1, IL-1β and IL-6 and for M2, IL-10 over 7 days; data was compared to TCP as a reference sample. (Mean ± SD, n = 3). *p < 0.05; **p < 0.01, ***p < 0.001.

likely mediated by altered cell shapes in response to distinct scaffolds configuration, which ultimately alters the fate commitment of hPDLSCs. This is in agreement with previous work where MSCs commitment was dependent upon changes in cell shape, cytoskeletal tension, and RhoA signaling in response to mechanical cues [39]. Specifically, aligned fibrous substrates show the ability to promote differentiation of cells into tendons/ligaments [40], whereas non-aligned fiber configuration permits cells to exhibit a more spread out morphology and direct osteogenic fate [17]. Taken together, according to our *in vitro* results, MEW PCL scaffolds with aligned fibers lead to the expression of ligamentogenic markers, which are essential for proper matrix formation and maturation of PDL *in vivo* [18].

3.3. Macrophage elongation and polarization depends on fiber orientation and scaffold architecture

To investigate the immunomodulatory effect via controlling scaffold architecture (strand spacing) and fiber configuration (aligned vs. random), RAW 264.7 cells (macrophages) were seeded on the defined scaffolds (Fig. 1). *E. coli* lipopolysaccharide (LPS), a well-known inducer of the expression of inflammatory markers, was added to culture media, and changes in the expression of macrophage phenotypical markers were determined by qPCR and ELISA. RAW 264.7 cells cultured on randomly-oriented fibrous scaffolds were able to maintain a round phenotype at day 1, while elongation of cells was more prominent when macrophages were cultured on aligned scaffolds (Fig. 5). Meanwhile, cell spreading and elongation remained comparable in non-stimulated and LPS-stimulated RAW 264.7 cells on all tested scaffolds (Fig. 5). Remarkably, even in an inflammation-stimulated *milieu*, fiber alignment and strand spacing tend to influence macrophage elongation, which is believed to promote changes in the expression of phenotypical markers from M1 to M2 [41]. It is known that the dynamic shift in phenotypes provided by the adjoining microenvironment, the so-called immunomodulatory approach reduces ongoing tissue damage and fosters alveolar bone regeneration [20,42]. As expected, cells cultured on scaffolds at different fiber configurations and strands spacing in non-stimulated condition failed to express the inflammatory markers IL-1β and IL-6 and were found to express M2 marker IL-10.

LPS-stimulated macrophages showed stronger upregulation for IL-1, in contrast, the expression of IL-6 was maintained at day 1 through day 7 despite continuous induction of LPS into the culture media. Meanwhile, stronger upregulation of IL-10 was also detected at day 1, potentially as an adaptive mechanism in LPS-stimulated macrophages in order to downregulate the expression of TNF-α, IL-1, and IL-6, proinflammatory cytokines [43–45]. At days 3 and 7, IL-10 continued to express at a significantly higher level in aligned and highly-ordered scaffolds with small and large strands spacing compared to control (tissue culture plate, TCP) ($P < 0.05$). Scaffolds with randomly-oriented fibers were not significantly different from the control (Fig. 6), in line with previous observations of the release of pro-inflammatory cytokines from macrophage cultures on 2D flat surface of poly(L-lactic) (PLLA) film and electrospun PLLA random scaffolds [46]. Taken together, our findings support the hypothesis that cell elongation might promote macrophage polarization and further release of M2 cytokines, although it maintains a constant level of the inflammatory cytokines over 7 days due to continuous induction of LPS into the culture medium.

Furthermore, the gene expression profiles in LPS-stimulated macrophages were evaluated over 7 days (Fig. 7). Overall, RAW 264.7 cells cultured on aligned and highly-ordered scaffolds with small and large strands spacing showed the upregulation of M2 Markers (IL-10 and MRC-1) and downregulation of the M1 markers (IL-1β) compared to randomly-oriented fibrous scaffolds and cells cultured on tissue culture plate. While the expression of IL-1β at days 3 and 7 was not significant in the groups tested, it was downregulated compared to the control. At day 7, the expression of MRC-1 was significantly downregulated in random fibers compared to aligned and small strand spacing scaffold design. It is believed that the M2 phenotype possesses distinct functionality from the M1 to upregulate the factors involved in repair and regeneration via stimulation of cell proliferation and deposition of ECM, as well as angiogenic effect [47]. Altogether, our data suggest that aligned fiber configuration and highly-ordered scaffold designs with small and large strand spacings promote macrophage polarization toward M2

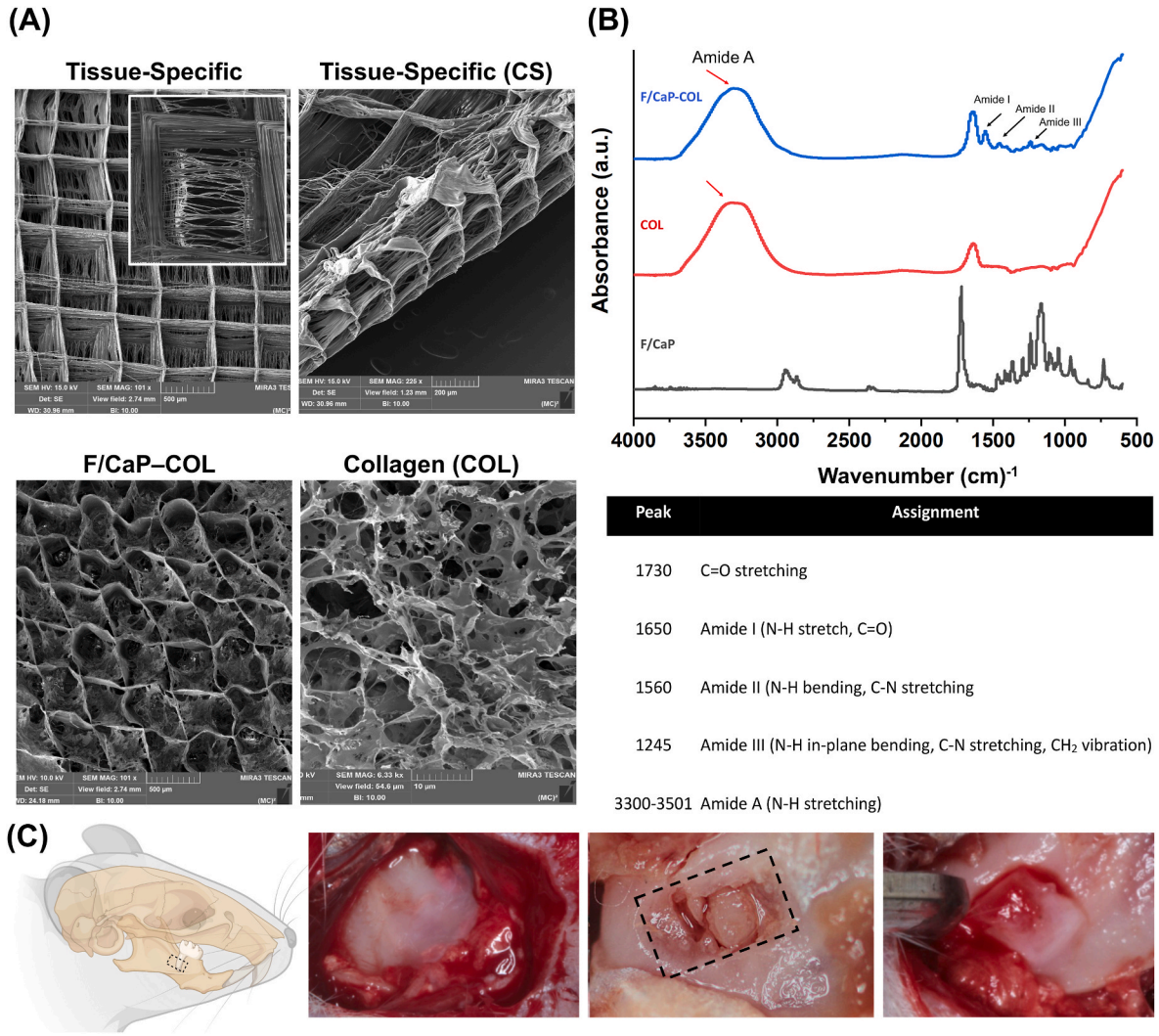

Fig. 8. Fabrication and characterization of tissue-specific zonal scaffolds. (A) Representative SEM images for tissue-specific scaffold with aligned PDL zone and 500 μm strands spacing for bone zone, and SEM images for collagen-infused scaffolds. **(B)** FTIR spectra of collagen, F/CaP-coated MEW PCL scaffold, and F/CaP-coated MEW PCL scaffold infused with collagen. Data show chemical functional groups related to phosphate at ~565 cm^{-1} and ~960 cm^{-1} in F/CaP-coated scaffolds, while collagen-infused scaffolds and collagen also show the amide groups, confirming successful permeation of collagen within the MEW scaffolds. (*) indicates the presence of PCL. **(C)** Generation of the rat mandibular periodontal fenestration model. Photographs of a rat mandible after the incision, flap elevation, creation of the defect, and implantation of tissue-specific scaffold in the defect region.

(pro-healing) phenotype.

3.4. Quantification of personalized scaffold printing accuracy

Advances in technology to combine image-based processing and 3D printing have enabled high-fidelity manufacturing of personalized scaffolds for anatomically-complex structures [9]. Nonetheless, most of the existing additive manufacturing approaches which have been employed to periodontal reconstruction present limitations of low resolution and bulky nature of the printed scaffolds [9]. Here, the fabrication of a defect-specific scaffold was demonstrated using MEW and 3D microCT imaging data of a standardized periodontal defect (Figs. S2A–B). Although the external geometry of the MEW printed scaffold tailored for the defect was determined to have an overall high printing accuracy of 0.7 ± 0.1 (Fig. S2C), the internal microstructural features were less accurate due to the reduced size of the defect. These results indicate the ability to deploy MEW in the challenging field of regenerative periodontics for the fabrication of personalized scaffolds in a clinical scale. However, further work is required to ensure high printing accuracy of the internal microstructure. Based on these results, we fabricated scaffolds with internal tissue specific microstructure while the external, defect-specific, scaffold macrostructure was trimmed to the implantation site by the surgeon.

3.5. In vivo evaluation of tissue-specific scaffold guidance for periodontal regeneration

To elucidate the importance of tissue-specific attributes, for instance fiber morphology (microarchitecture), strand spacing (macroarchitecture), and chemical composition (F/CaP nanostructured coating) in the generation of defect-specific (personalized) zonal scaffolds for periodontal regeneration, 3D MEW polymeric (PCL) scaffolds were designed and fabricated via MEW. Worth mentioning, concerning the bone zone, we followed our group's most recent investigation, in which we detailed the fabrication of a novel nanostructured fluorinated calcium phosphate (F/CaP) MEW PCL scaffold. Meanwhile, in the present study, we aimed at identifying the most suitable scaffold architecture and fiber configuration (PDL zone) to concomitantly support periodontal ligament (PDL) regeneration. Of note, knowing that one of the primary functions of scaffolds for periodontal regeneration is to

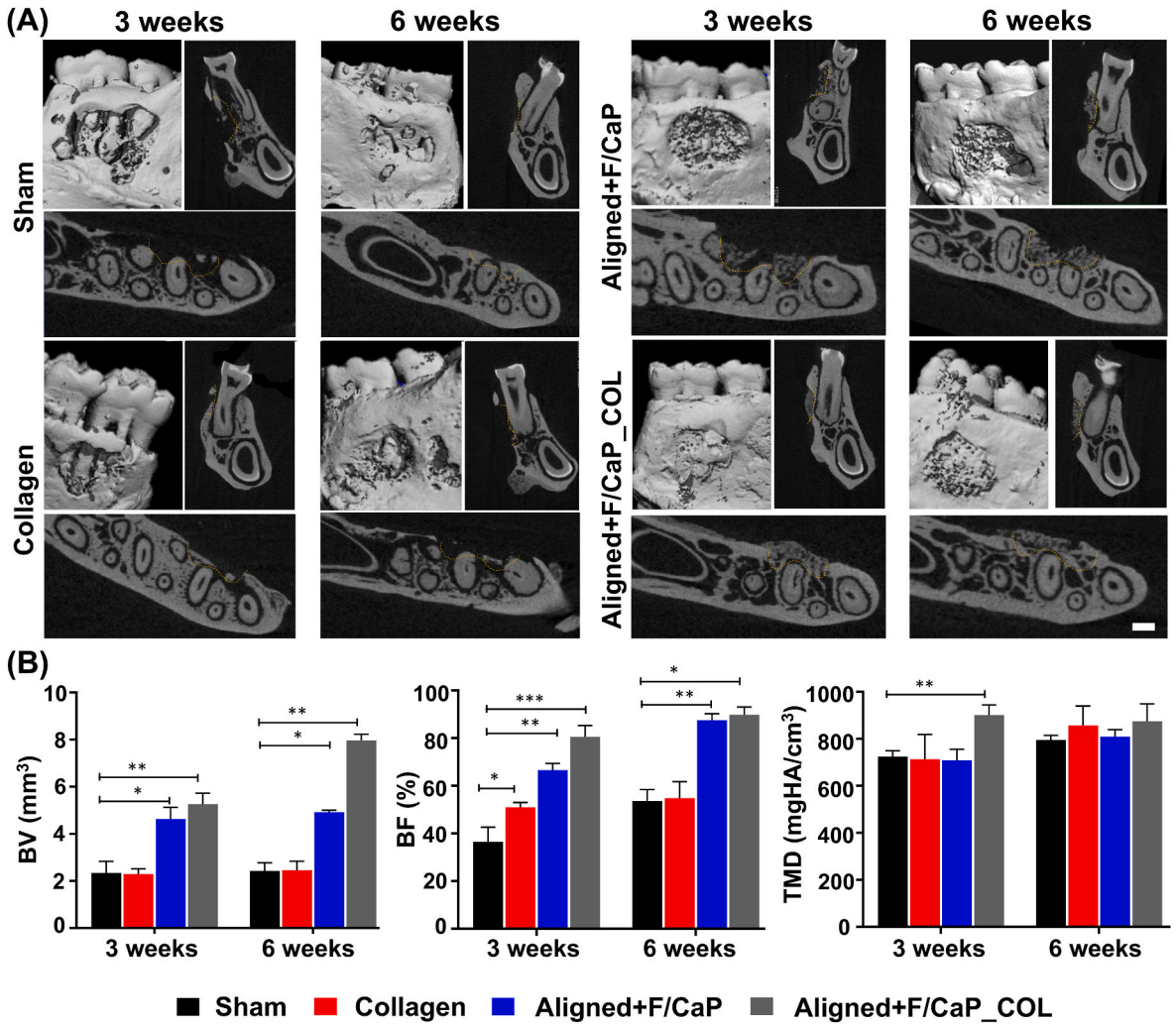

Fig. 9. MicroCT assessment of bone formation. (A) Representative microCT images of the fenestration defect exposing the distal root of the second molar at 3 and 6 weeks in the Control (Sham), Collagen, and Biphasic scaffold with Aligned (PDL) compartment and non-coated and coated (F/CaP) and aligned and coated (F/CaP) + collagen. Transverse views highlight the visual differences between the area and density of bone regenerated within the defect. (Scale bar = 1 mm). **(B)** μCT assessments of bone volume, bone fill, and tissue mineral density at 3 and 6 weeks after surgery, within the different groups. The coated (F/CaP) group and the presence of collagen further show significant differences for bone volume and bone fill compared to both the control and non-coated groups. Mean ± SD (n = 6). ANOVA: *p < 0.05; **p < 0.01.

hamper soft tissue penetration into the defect, we hypothesized that the infusion of collagen within the macroporous structure of the tissue-specific zonal scaffold could provide a temporary barrier to the fast invasion of gingival epithelium and fibroblasts, and thus, optimize the regenerative capacity of the developed scaffold.

The fabricated tissue-specific scaffolds exhibited distinct fibers' orientation (Fig. 8A). In particular, SEM analysis demonstrates aligned fibers for the designed PDL zone at ~200 μm height resembling those of native PDL space and a highly-ordered (0/90° crosshatch) and porous (500 μm strand spacing) for the bone zone at ~800 μm height. As formerly highlighted, the bone zone of the tissue-specific scaffold was subjected to our previously developed F/CaP coating. Furthermore, SEM analysis of collagen-infused scaffolds shows uniform collagen infiltration into the porous MEW PCL zonal scaffolds. Collagen type I, upon dissolving in acetic acid, exhibits a low viscosity that turns upon neutralization and temperature control to exhibit self-assembly and hydrogen bond to form a gel. The presence of specific chemical groups coding for F/CaP-coated PCL scaffold, collagen, and collagen-infused scaffolds was used to determine successful integration of F/CaP-coated scaffolds with collagen (Fig. 8B). The FTIR spectra of the F/CaP-coated scaffolds confirmed vibrational bands from PCL at 2943 cm^{-1}, 2866 cm^{-1}, and 1700 cm^{-1}, which is consistent with previous findings [15]. Additionally, the collagen-infused zonal scaffold showed vibrational bands at 1650 cm^{-1}, 1540 cm^{-1}, and 3310 cm^{-1} attributed to the infused collagen [15]. Together, the SEM and FTIR analyses suggest effective fabrication of collagen-infused scaffolds without altering the composition of the base materials used.

The potential of the engineered fibrous scaffolds to support neotissue deposition was evaluated using a well-established periodontal fenestration defect model in rat mandible (Fig. 8C). According to our histological and immunohistochemical findings, the compositional (*i.e.*, F/CaP coating) and structural organization (fiber alignment) of the fabricated zonal scaffolds resulted in concurrent regeneration of alveolar bone and PDL (Fig. 9). The microCT analysis revealed substantial differences in bone formation at defect sites among the investigated scaffold groups. The control group showed partial tissue healing even after 6 weeks and was comparable to the collagen-treated group. While the tissue-specific zonal scaffolds (with and without collagen infiltration) showed pronounced bone healing, the collagen-infused counterpart demonstrated a more advanced formation of mineralized tissue at both time points (3 and 6 weeks) (Fig. 9A). Pertinent to periodontal tissue regeneration, abundant formation of new bone (BV and BF) with proper

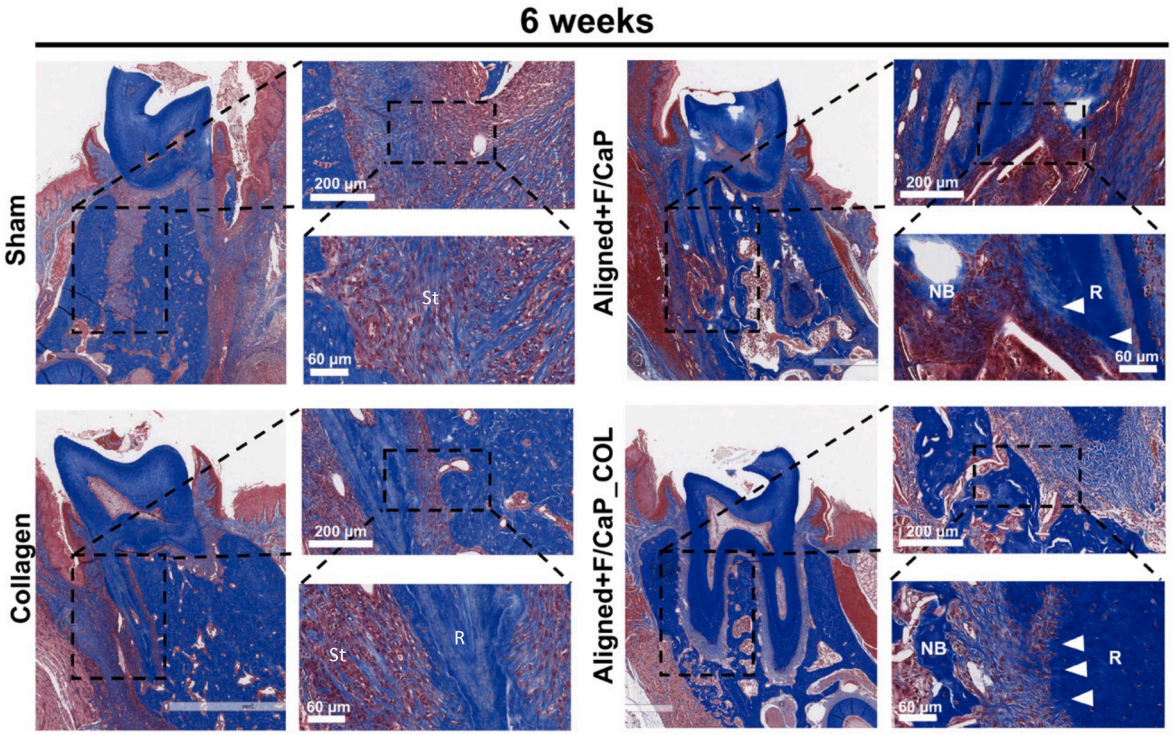

Fig. 10. Masson's trichrome staining of periodontal defects treated with the distinct scaffolds and evaluated after 6 weeks post-scaffolds implantation. Representative Masson's trichrome-stained horizontal cross-section of Control (Sham), Collagen, and tissue specific scaffolds with aligned fiber configuration (PDL) compartment and coated (F/CaP) fibers (bone compartment) and tissue specific scaffold infused with collagen at 6-weeks post-implantation. Yellow dashed line highlights the area of scaffold placement and new bone formation. White arrowhead for PDL, NB: new bone; R: Root surface; St: Soft tissue.

PDL space was observed and was statistically significant in the tissue-specific scaffolds compared to sham (no treatment, defect only) and collagen groups (Fig. 9B). Tissue mineral density (TMD) demonstrating maturity of bone showed a significant difference ($p < 0.001$) between tissue-specific scaffolds infused with collagen versus the other groups at 3 weeks. Although at 6 weeks no differences in TMD between groups were detected. The enhanced bone formation can be attributed to the 500 μm strand spacing, which was sufficient to support mineralized tissue formation due to improved vascularization and further, due to the presence of the F/CaP coating that stimulates mineralized tissue deposition [15]. In agreement with Abbasi et al., a pore size of 500 μm resulted in the highest formation of new bone compared to a smaller (250 μm) pore size [48].

Histological evaluation of the newly-formed periodontal tissues revealed a substantial influence of the proposed tissue-specific zonal scaffold (*i.e.*, aligned/F–CaP coated scaffold) in the regenerative capacity (Fig. 10) and (Fig. S3). In detail, while the control group showed soft tissue invasion because of epithelial tissue down growth; collagen alone failed to promote the regeneration of both hard and soft periodontal tissues. Remarkably, our tissue-specific zonal scaffold provides guidance for tissue formation and the amount of new bone formation was higher in aligned/F–CaP coated scaffolds compared to sham (control) and collagen groups. Interestingly, both tissue-specific zonal scaffolds (with and without collagen infusion) maintained PDL space that resembles those of natural periodontal tissue (Fig. 10). Worth mentioning, our *in vivo* investigation was limited to 6 weeks, and we did not try to evaluate the mechanical properties of the regenerated periodontal ligament tissue. A previous work by Pilipchuck et al., 2018, highlighted that even after 9 weeks of scaffold implantation, the newly formed PDL did not reach a statistically significant difference in stiffness when compared to native tissue properties [18]. Nevertheless, although we did not evaluate the biomechanical properties of the regenerated tissues to further emphasize the influence of the scaffold's well-defined macroarchitecture (*i.e.*, strand spacing), composition (F/CaP coating), and microstructural features (fiber alignment), the collected *in vivo* data (histological and immunohistochemical) were sufficient to show the efficacy of the tissue-specific scaffold to form and regenerate the periodontium. Importantly, our prior work on the development of the nanostructured F/CaP-coated MEW PCL scaffolds [15] reports on the effects of our novel coating on the scaffolds' mechanical properties. Overall, F/CaP-coated MEW PCL scaffolds show enhanced tensile strength and Young's modulus compared to their noncoated (NaOH etched) and pristine counterparts. Future studies are warranted to address not only the biomechanics of the regenerated tissues but also the scaffold performance and overall integrity under cyclic (masticatory) loading.

It is well-established that the integration of polarized anchoring fibers oriented toward a mineralizing surface promotes adequate maturation and exhibits important biomechanical properties to regulate tissue adaptability and its long-term stability [49]. Herein, while monophasic (*i.e.*, single zone/bone) F/CaP-coated MEW PCL scaffolds might allow tissue regeneration, as we previously reported [15], recent research suggests that forming the angular structure of PDL at the bone-ligament interface would be nearly impossible, and the result will not be true regeneration of the lost structures. Aiming to unveil the regenerative capacity of novel MEW tissue-specific zonal scaffolds, our immunohistochemical findings show that the newly formed PDL tissue displayed mature structures for the groups with tissue-specific (aligned fiber configuration for PDL and F/CaP-coated 500 μm strand spacing for bone) attributes (Fig. S4), regardless of the collagen presence. Importantly, periostin (POSTN) expression has been paired with PDL maturation to establish homeostasis within periodontal tissues [18]. At 6 weeks, the defects treated with the tissue-specific zonal scaffolds showed higher POSTN expression similar to the contralateral (untouched) remaining intact PDL area of the same tooth (Fig. S4). Of note, analysis of Sharpey's fibers varied according to positions, fiber groups, sides, and

teeth, with a significant difference between bone and cementum side [50]. Interestingly, despite the amount of bone regeneration being higher in the collagen-infused tissue-specific scaffolds due to improved vascularization as noted previously [15], lower expression of POSTN is evident compared to collagen-free tissue-specific scaffolds. These *in vivo* findings are likely attributed to the physical enveloping of the aligned fibers, thus precluding the guidance effect for optimizing PDL tissue neoformation as demonstrated in defects treated with the tissue-specific scaffold devoid of collagen that was sufficient to reestablish mature PDL (Fig. S4).

4. Conclusions

In summary, our findings provide evidence of morphological and functional changes in response to scaffold architecture (strand spacing), fiber configuration, and composition (F/CaP coating). Specifically, aligned fibers strongly support ligamentogenesis whereas highly-ordered scaffold architecture with strands spacing of 500 μm supports osteogenesis, which has not been reported within the context of periodontal tissue engineering. Moreover, fiber orientation and strands spacing were found to directly correlate to the morphological elongation of macrophages and differentiation toward the pro-healing M2 phenotype. The *in vivo* findings confirmed that a structurally tailored scaffold with a PDL zone formed by highly-oriented (aligned) MEW PCL fibers and a bone zone consisted of F/CaP-coated MEW PCL fibers displaying 500 μm strand spacing allowed for coordinated periodontal tissue regeneration in a well-established (*i.e.*, surgically removes alveolar bone, cementum and soft tissue components around the tooth root) rodent mandibular fenestration defect model. Altogether, our findings demonstrate that MEW could ultimately lead to the development of zonal biomaterial-mediating scaffolds capable of directing tissue-specific stem cell differentiation and macrophage polarization. This approach could be used as a personalized therapy for effective tissue regeneration in inflammatory-driven diseases such as periodontitis. Future studies to evaluate the effect of macrophage polarization in response to tissue-specific zonal scaffolds and the effects on periodontal tissue regeneration under inflammatory *in vivo* conditions are warranted. In addition, we are considering future work to be conducted in large animals (*e.g.*, canine or porcine) models, to validate the role of the tissue-specific scaffolds engineered in this study using a clinically relevant model.

CRediT authorship contribution statement

Arwa Daghrery: Conceptualization, Investigation, Methodology, Formal analysis, Data curation, Visualization, Writing – original draft. **Jessica A. Ferreira:** Investigation, Methodology, Formal analysis. **Jinping Xu:** Investigation, Methodology, Formal analysis. **Nasim Golafshan:** Investigation, Methodology, Formal analysis, Writing – review & editing. **Darnell Kaigler:** Methodology, Writing – review & editing. **Sarit B. Bhaduri:** Writing – review & editing. **Jos Malda:** Writing – review & editing. **Miguel Castilho:** Investigation, Methodology, Formal analysis, Supervision, Writing – review & editing. **Marco C. Bottino:** Conceptualization, Writing – review & editing, Supervision, Funding acquisition, Project administration.

Declaration of competing interest

The authors declare no conflict of interest.

Acknowledgments

M.C.B. acknowledges the National Institutes of Health (NIH – National Institute of Dental and Craniofacial Research, grants K08DE023552 and R01DE026578). M.C.B. and S.B.B. are grateful for funds received from the Osteo Science Foundation (Peter Geistlich Research Award) and the American Academy of Implant Dentistry Foundation (AAIDF). S.B.B. acknowledges support from the National Science Foundation (NSF IR/D program). J.M. and M.C. acknowledge the financial support from the Gravitation Program "Materials Driven Regeneration", funded by the Netherlands Organization for Scientific Research (024.003.013), and the partners of Regenerative Medicine Crossing Borders and powered by Health Holland, Top Sector Life Sciences & Health, the Netherlands. M.C. acknowledges the financial support from the Reprint project (OCENW.XS5.161) by the Netherlands Organization for Scientific Research. The authors are indebted to Mariane M. Azuma for providing input in ELISA assays and macrophages experiments. The content is solely the responsibility of the authors and does not necessarily represent the official views of the NIH and NSF.

Appendix A. Supplementary data

Supplementary data to this article can be found online at https://doi.org/10.1016/j.bioactmat.2022.04.013.

References

[1] P.I. Eke, B.A. Dye, L. Wei, G.O. Thornton-Evans, R.J. Genco, Prevalence of periodontitis in adults in the United States: 2009 and 2010, J. Dent. Res. 91 (2012) 914–920, https://doi.org/10.1177/0022034512457373.
[2] S. Ivanovski, C. Vaquette, S. Gronthos, D.W. Hutmacher, P.M. Bartold, Multiphasic scaffolds for periodontal tissue engineering, J. Dent. Res. 93 (2014) 1212–1221, https://doi.org/10.1177/0022034514544301.
[3] Z. Aytac, N. Dubey, A. Daghrery, J.A. Ferreira, I.J. de S. Araújo, M. Castilho, J. Malda, M.C. Bottino, Innovations in craniofacial bone and periodontal tissue engineering – from electrospinning to converged biofabrication, Int. Mater. Rev. (2021) 1–38, https://doi.org/10.1080/09506608.2021.1946236, 0.
[4] G. Pellegrini, G. Pagni, G. Rasperini, Surgical approaches based on biological objectives: GTR versus GBR techniques, Int J Dent 2013 (2013), https://doi.org/10.1155/2013/521547.
[5] M. Kaku, M. Yamauchi, Mechano-regulation of collagen biosynthesis in periodontal ligament, J Prosthodont Res 58 (2014) 193–207, https://doi.org/10.1016/j.jpor.2014.08.003.
[6] Q.C. Peiffer, M. de Ruijter, J. van Duijn, D. Crottet, E. Dominic, J. Malda, M. Castilho, Melt electrowriting onto anatomically relevant biodegradable substrates: resurfacing a diarthrodial joint, Mater. Des. 195 (2020), 109025, https://doi.org/10.1016/j.matdes.2020.109025.
[7] Y. Liang, X. Luan, X. Liu, Recent advances in periodontal regeneration: a biomaterial perspective, Bioact. Mater. 5 (2020) 297–308, https://doi.org/10.1016/j.bioactmat.2020.02.012.
[8] H.N. Woo, Y.J. Cho, S. Tarafder, C.H. Lee, The recent advances in scaffolds for integrated periodontal regeneration, Bioact. Mater. 6 (2021) 3328–3342, https://doi.org/10.1016/j.bioactmat.2021.03.012.
[9] G. Rasperini, S.P. Pilipchuk, C.L. Flanagan, C.H. Park, G. Pagni, S.J. Hollister, W. V. Giannobile, 3D-printed bioresorbable scaffold for periodontal repair, J. Dent. Res. 94 (2015), https://doi.org/10.1177/0022034515588303, 153S–7S.
[10] P.F. Costa, C. Vaquette, Q. Zhang, R.L. Reis, S. Ivanovski, D.W. Hutmacher, Advanced tissue engineering scaffold design for regeneration of the complex hierarchical periodontal structure, J. Clin. Periodontol. 41 (2014) 283–294, https://doi.org/10.1111/jcpe.12214.
[11] P.T. Sudheesh Kumar, S. Hashimi, S. Saifzadeh, S. Ivanovski, C. Vaquette, Additively manufactured biphasic construct loaded with BMP-2 for vertical bone regeneration: a pilot study in rabbit, Mater Sci Eng C Mater Biol Appl 92 (2018) 554–564, https://doi.org/10.1016/j.msec.2018.06.071.
[12] C. Vaquette, J. Mitchell, T. Fernandez-Medina, S. Kumar, S. Ivanovski, Resorbable additively manufactured scaffold imparts dimensional stability to extraskeletally regenerated bone, Biomaterials 269 (2021), 120671, https://doi.org/10.1016/j.biomaterials.2021.120671.
[13] C. Vaquette, S. Saifzadeh, A. Farag, D.W. Hutmacher, S. Ivanovski, Periodontal tissue engineering with a multiphasic construct and cell sheets, J. Dent. Res. 98 (2019) 673–681, https://doi.org/10.1177/0022034519837967.
[14] A. Daghrery, I.J. de Souza Araújo, M. Castilho, J. Malda, M.C. Bottino, Unveiling the potential of melt electrowriting in regenerative dental medicine, Acta Biomater. (2022), https://doi.org/10.1016/j.actbio.2022.01.010. In press.
[15] A. Daghrery, J.A. Ferreira, I.J. de Souza Araújo, B.H. Clarkson, G.J. Eckert, S. B. Bhaduri, J. Malda, M.C. Bottino, A highly ordered, nanostructured fluorinated CaP-coated melt electrowritten scaffold for periodontal tissue regeneration, Adv Healthc Mater (2021), e2101152, https://doi.org/10.1002/adhm.202101152.
[16] N. Dubey, J.A. Ferreira, A. Daghrery, Z. Aytac, J. Malda, S.B. Bhaduri, M. C. Bottino, Highly tunable bioactive fiber-reinforced hydrogel for guided bone regeneration, Acta Biomater. 113 (2020) 164–176, https://doi.org/10.1016/j.actbio.2020.06.011.
[17] N. Abbasi, S. Ivanovski, K. Gulati, R.M. Love, S. Hamlet, Role of offset and gradient architectures of 3-D melt electrowritten scaffold on differentiation and mineralization of osteoblasts, Biomater. Res. 24 (2020) 2, https://doi.org/10.1186/s40824-019-0180-z.

[18] S.P. Pilipchuk, T. Fretwurst, N. Yu, L. Larsson, N.M. Kavanagh, F. Asa'ad, K.C. K. Cheng, J. Lahann, W.V. Giannobile, Micropatterned scaffolds with immobilized growth factor genes regenerate bone and periodontal ligament-like tissues, Adv Healthc Mater 7 (2018), e1800750, https://doi.org/10.1002/adhm.201800750.
[19] C.H. Park, K.-H. Kim, Y.-M. Lee, W.V. Giannobile, Y.-J. Seol, 3D printed, microgroove pattern-driven generation of oriented ligamentous architectures, Int. J. Mol. Sci. 18 (2017), https://doi.org/10.3390/ijms18091927.
[20] T. Tylek, C. Blum, A. Hrynevich, K. Schlegelmilch, T. Schilling, P.D. Dalton, J. Groll, Precisely defined fiber scaffolds with 40 μm porosity induce elongation driven M2-like polarization of human macrophages, Biofabrication 12 (2020), 025007, https://doi.org/10.1088/1758-5090/ab5f4e.
[21] B.N. Brown, B.D. Ratner, S.B. Goodman, S. Amar, S.F. Badylak, Macrophage polarization: an opportunity for improved outcomes in biomaterials and regenerative medicine, Biomaterials 33 (2012) 3792–3802, https://doi.org/10.1016/j.biomaterials.2012.02.034.
[22] J.A. Ferreira, K.Z. Kantorski, N. Dubey, A. Daghrery, J.C. Fenno, Y. Mishina, H.-L. Chan, G. Mendonça, M.C. Bottino, Personalized and defect-specific antibiotic-laden scaffolds for periodontal infection ablation, ACS Appl. Mater. Interfaces 13 (2021) 49642–49657, https://doi.org/10.1021/acsami.1c11787.
[23] J. Visser, F.P.W. Melchels, J.E. Jeon, E.M. van Bussel, L.S. Kimpton, H.M. Byrne, W. J.A. Dhert, P.D. Dalton, D.W. Hutmacher, J. Malda, Reinforcement of hydrogels using three-dimensionally printed microfibres, Nat. Commun. 6 (2015) 1–10, https://doi.org/10.1038/ncomms7933.
[24] S. Yeasmin, J. Ceccarelli, M. Vigen, B. Carrion, A.J. Putnam, S.A. Tarle, D. Kaigler, Stem cells derived from tooth periodontal ligament enhance functional angiogenesis by endothelial cells, tissue eng Part A. https://doi.org/10.1089/ten.tea.2013.0512, 2014, 20, 1188, 1196.
[25] M. Dominici, K. Le Blanc, I. Mueller, I. Slaper-Cortenbach, F. Marini, D. Krause, R. Deans, A. Keating, D. Prockop, E. Horwitz, Minimal criteria for defining multipotent mesenchymal stromal cells. The International Society for Cellular Therapy position statement, Cytotherapy 8 (2006) 315–317, https://doi.org/10.1080/14653240600855905.
[26] N. Golafshan, K. Willemsen, F.B. Kadumudi, E. Vorndran, A. Dolatshahi-Pirouz, H. Weinans, B.C.H. van der Wal, J. Malda, M. Castilho, 3D-Printed Regenerative Magnesium Phosphate Implant Ensures Stability and Restoration of Hip Dysplasia, Advanced Healthcare Materials. n/a (n.d.) 2101051. https://doi.org/10.1002/adhm.202101051.
[27] A. Daghrery, Z. Aytac, N. Dubey, L. Mei, A. Schwendeman, M.C. Bottino, Electrospinning of dexamethasone/cyclodextrin inclusion complex polymer fibers for dental pulp therapy, Colloids Surf. B Biointerfaces (2020), 111011, https://doi.org/10.1016/j.colsurfb.2020.111011.
[28] P.D. Dalton, D. Grafahrend, K. Klinkhammer, D. Klee, M. Möller, Electrospinning of polymer melts: phenomenological observations, Polymer 48 (2007) 6823–6833, https://doi.org/10.1016/j.polymer.2007.09.037.
[29] B.-M. Seo, M. Miura, S. Gronthos, P. Mark Bartold, S. Batouli, J. Brahim, M. Young, P. Gehron Robey, C.Y. Wang, S. Shi, Investigation of multipotent postnatal stem cells from human periodontal ligament, Lancet 364 (2004) 149–155, https://doi.org/10.1016/S0140-6736(04)16627-0.
[30] K. Mrozik, S. Gronthos, S. Shi, P.M. Bartold, A method to isolate, purify, and characterize human periodontal ligament stem cells, in: G.J. Seymour, M. P. Cullinan, N.C.K. Heng (Eds.), Oral Biology: Molecular Techniques and Applications, Springer, New York, NY, 2017, pp. 413–427, https://doi.org/10.1007/978-1-4939-6685-1_24.
[31] Z. Zhao, J. Liu, M.D. Weir, N. Zhang, L. Zhang, X. Xie, C. Zhang, K. Zhang, Y. Bai, H.H.K. Xu, Human periodontal ligament stem cells on calcium phosphate scaffold delivering platelet lysate to enhance bone regeneration, RSC Adv. 9 (2019) 41161–41172, https://doi.org/10.1039/C9RA08336G.
[32] M. Suhaeri, R. Subbiah, S.-H. Kim, C.-H. Kim, S.J. Oh, S.-H. Kim, K. Park, Novel platform of cardiomyocyte culture and coculture via fibroblast-derived matrix-coupled aligned electrospun nanofiber, ACS Appl. Mater. Interfaces 9 (2017) 224–235, https://doi.org/10.1021/acsami.6b14020.
[33] S. Ren, Y. Yao, H. Zhang, R. Fan, Y. Yu, J. Yang, R. Zhang, C. Liu, W. Sun, L. Miao, Aligned fibers fabricated by near-field electrospinning influence the orientation and differentiation of hPDLSCs for periodontal regeneration, J. Biomed. Nanotechnol. 13 (2017) 1725–1734, https://doi.org/10.1166/jbn.2017.2451.
[34] C.H. Lee, H.J. Shin, I.H. Cho, Y.-M. Kang, I.A. Kim, K.-D. Park, J.-W. Shin, Nanofiber alignment and direction of mechanical strain affect the ECM production of human ACL fibroblast, Biomaterials 26 (2005) 1261–1270, https://doi.org/10.1016/j.biomaterials.2004.04.037.
[35] W. Jiang, L. Li, D. Zhang, S. Huang, Z. Jing, Y. Wu, Z. Zhao, L. Zhao, S. Zhou, Incorporation of aligned PCL–PEG nanofibers into porous chitosan scaffolds improved the orientation of collagen fibers in regenerated periodontium, Acta Biomater. 25 (2015) 240–252, https://doi.org/10.1016/j.actbio.2015.07.023.
[36] H.F. Rios, D. Ma, Y. Xie, W.V. Giannobile, L.F. Bonewald, S.J. Conway, J.Q. Feng, Periostin is essential for the integrity and function of the periodontal ligament during occlusal loading in mice, J. Periodontol. 79 (2008) 1480–1490, https://doi.org/10.1902/jop.2008.070624.
[37] A. Takimoto, M. Kawatsu, Y. Yoshimoto, T. Kawamoto, M. Seiryu, T. Takano-Yamamoto, Y. Hiraki, C. Shukunami, Scleraxis and osterix antagonistically regulate tensile force-responsive remodeling of the periodontal ligament and alveolar bone, Development 142 (2015) 787–796, https://doi.org/10.1242/dev.116228.
[38] N. Yu, L. Prodanov, J. te Riet, F. Yang, X.F. Walboomers, J.A. Jansen, Regulation of periodontal ligament cell behavior by cyclic mechanical loading and substrate nanotexture, J. Periodontol. 84 (2013) 1504–1513, https://doi.org/10.1902/jop.2012.120513.
[39] R. McBeath, D.M. Pirone, C.M. Nelson, K. Bhadriraju, C.S. Chen, Cell shape, cytoskeletal tension, and RhoA regulate stem cell lineage commitment, Dev. Cell 6 (2004) 483–495, https://doi.org/10.1016/s1534-5807(04)00075-9.
[40] Z. Yin, X. Chen, J.L. Chen, W.L. Shen, T.M. Hieu Nguyen, L. Gao, H.W. Ouyang, The regulation of tendon stem cell differentiation by the alignment of nanofibers, Biomaterials 31 (2010) 2163–2175, https://doi.org/10.1016/j.biomaterials.2009.11.083.
[41] F.Y. McWhorter, T. Wang, P. Nguyen, T. Chung, W.F. Liu, Modulation of macrophage phenotype by cell shape, Proc. Natl. Acad. Sci. Unit. States Am. 110 (2013) 17253–17258, https://doi.org/10.1073/pnas.1308887110.
[42] Z. Hu, C. Ma, X. Rong, S. Zou, X. Liu, Immunomodulatory ECM-like microspheres for accelerated bone regeneration in diabetes mellitus, ACS Appl. Mater. Interfaces 10 (2018) 2377–2390, https://doi.org/10.1021/acsami.7b18458.
[43] C.-H. Wu, T.-L. Chen, T.-G. Chen, W.-P. Ho, W.-T. Chiu, R.-M. Chen, Nitric oxide modulates pro- and anti-inflammatory cytokines in lipopolysaccharide-activated macrophages, J. Trauma Acute Care Surg. 55 (2003) 540–545, https://doi.org/10.1097/01.TA.0000033496.62796.3B.
[44] D.F. Fiorentino, A. Zlotnik, P. Vieira, T.R. Mosmann, M. Howard, K.W. Moore, A. O'Garra, IL-10 acts on the antigen-presenting cell to inhibit cytokine production by Th1 cells, J. Immunol. 146 (1991) 3444–3451.
[45] I.P. Oswald, T.A. Wynn, A. Sher, S.L. James, Interleukin 10 inhibits macrophage microbicidal activity by blocking the endogenous production of tumor necrosis factor alpha required as a costimulatory factor for interferon gamma-induced activation, Proc. Natl. Acad. Sci. U. S. A. 89 (1992) 8676–8680, https://doi.org/10.1073/pnas.89.18.8676.
[46] E. Saino, M.L. Focarete, C. Gualandi, E. Emanuele, A.I. Cornaglia, M. Imbriani, L. Visai, Effect of electrospun fiber diameter and alignment on macrophage activation and secretion of proinflammatory cytokines and chemokines, Biomacromolecules 12 (2011) 1900–1911, https://doi.org/10.1021/bm200248h.
[47] C. Atri, F.Z. Guerfali, D. Laouini, Role of human macrophage polarization in inflammation during infectious diseases, Int. J. Mol. Sci. 19 (2018), https://doi.org/10.3390/ijms19061801.
[48] N. Abbasi, R.S.B. Lee, S. Ivanovski, R.M. Love, S. Hamlet, In vivo bone regeneration assessment of offset and gradient melt electrowritten (MEW) PCL scaffolds, Biomater. Res. 24 (2020) 17, https://doi.org/10.1186/s40824-020-00196-1.
[49] C.H. Park, H.F. Rios, Q. Jin, J.V. Sugai, M. Padial-Molina, A.D. Taut, C.L. Flanagan, S.J. Hollister, W.V. Giannobile, Tissue engineering bone-ligament complexes using fiber-guiding scaffolds, Biomaterials 33 (2012) 137–145, https://doi.org/10.1016/j.biomaterials.2011.09.057.
[50] Y. Liang, Z. Hu, B. Chang, X. Liu, Quantitative characterizations of the Sharpey's fibers of rat molars, J. Periodontal. Res. 55 (2020) 307–314, https://doi.org/10.1111/jre.12716.